WEGC Technical Report for ESA/ESTEC No. 1/2013 — AEXPWIND TN3-Part1

Project AEXPWIND: Trace Gas Retrieval and Performance of Wind and Greenhouse Gas Profiling in the Irdas-Exp/Accurate Context

[ESA ESTEC Contract No. 4000105679/12/NL/CBi]

Formulation and analysis of an Abel transform for deriving line-of-sight wind profiles from LEO-LEO IR laser occultation

S. Syndergaard (WEGC Consultant, Copenhagen, DK) and
G. Kirchengast (WEGC AEXPWIND team, Univ. of Graz, AT)

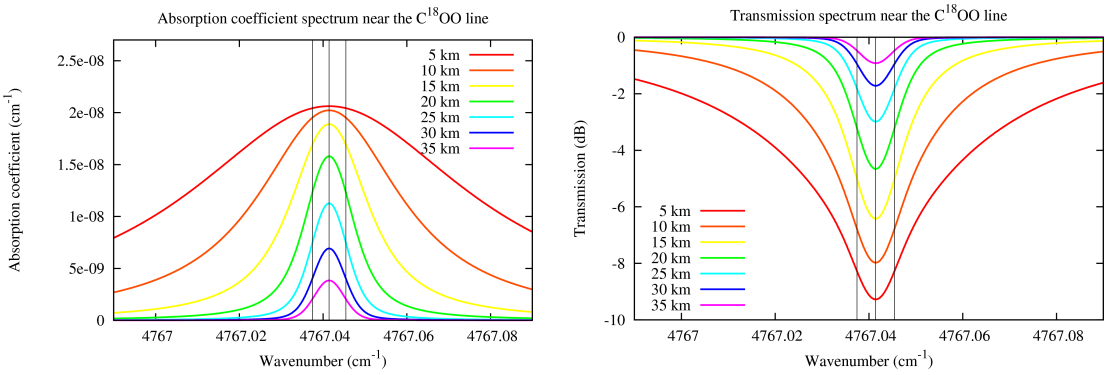

June 2013 (final version)
Wegener Center for Climate and Global Change (WEGC)
University of Graz

Acronyms and Abbreviations

3D	Three-dimensional
ACCURATE	Atmospheric Climate and Chemistry in the UTLS Region and climate Trends Explorer
AEXPWIND	Trace Gas Retrieval and Performance of Wind and Greenhouse Gas Profiling in the Irdas-Exp/Accurate Context
ECEF	Earth Centered Earth Fixed
EGOPS	End-to-End Generic Occultation Performance Simulation and Processing System
ESA	European Space Agency
GNSS	Global Navigation Satellite System
IR	Infra-red
IRDAS-EXP	SWIR Long Range Differential Absorption Experiment for Trace Gas Measurements
LEO	Low Earth Orbit
LIO	LEO-LEO IR Laser Occultation
l.o.s.	Line-of-sight
HITRAN	High-resolution Transmission (molecular absorption database)
SWIR	Short-Wave Infrared
TPH	Tangent Point Height
UTLS	Upper Troposphere Lower Stratosphere
WEGC	Wegener Center for Climate and Global Change
xEGOPS	Experimental EGOPS

Contents

1 Introduction

The objective of this study is to develop, in line with the AEXPWIND proposal [1], an Abel transform for the retrieval of the line-of-sight (l.o.s.) wind from future satellite-to-satellite Infrared (IR) laser occultation measurements [2]. Theoretical considerations are made in Section 2, and a couple of alternative transforms are developed and analysed. Assessment of errors and approximations are made using numerical simulations in Section 3. Conclusions are drawn in Section 4.

2 Theoretical considerations

2.1 Considerations about Doppler shifts

2.1.1 Doppler shift due to motion of the transmitter

A transmitter in a Low Earth Orbit (LEO) typically moves at a speed, v_{Tx}, of about 7500 m/s. For the frequencies of interest here ($f \approx 1.5 \times 10^{14}$ Hz; wavelength $\lambda \approx 2\,\mu$m), this gives rise to a relative Doppler shift of the transmitted signal on the order of

$$\frac{\Delta f}{f} \sim \frac{v_{\mathrm{Tx}}}{c} \approx 2.5 \times 10^{-5}, \tag{2.1}$$

where c is the speed of light, and $\Delta f = f - f_{\mathrm{Tx}}$, f_{Tx} being the frequency generated internally by the transmitter.

2.1.2 Doppler shift due to Earth's rotation

Without any wind, it is the frequency in the ECEF (Earth Centered Earth Fixed) frame that is relevant to the species absorption. Thus the rotation of Earth also induces a Doppler shift depending on latitude and propagation direction of the signal. At the Equator the speed of rotation, v_Ω, is about 464 m/s, potentially giving rise to a relative Doppler shift of about

$$\frac{\Delta f}{f} \sim \frac{v_\Omega}{c} \approx 1.5 \times 10^{-6}. \tag{2.2}$$

In practice, for a near polar orbit, the Doppler shift due to the Earth rotation would be considerably smaller, but generally not negligible; it is always determined by the projection of the local velocity of rotation onto the propagation direction.

2.1.3 Doppler shift due to wind

The part of the wind that would be measurable with LIO (LEO-LEO IR Laser Occultation) during an occultation event (mostly meridional component because of the occultation geometry and near polar orbits) would have a maximum speed of several 10 m/s for which we can take 30 m/s as a well representative speed [3; 2]. Such a l.o.s. wind speed, v_{ll}, gives rise to a relative Doppler shift of about

$$\frac{\Delta f}{f} \sim \frac{v_{\mathrm{ll}}}{c} \approx 1 \times 10^{-7}. \tag{2.3}$$

For comparison, the separation between the anticipated frequencies to be used for wind measurements near the line center of the $C^{18}OO$ absorption line (line center at $f/c = 4767.041455\,\mathrm{cm}^{-1}$) is about 1.6×10^{-6} [3; 2]. Thus, both the transmitter velocity and the Earth's rotation must be accounted for upon transmission of the signals such that

the effective frequency felt by the absorbing molecules are close to the desired ones. In essence it is the velocity of the transmitter in the ECEF frame projected on to the propagation direction (also in the ECEF frame) that is important, and the transmitter would have to be able to adjust the internally generated frequencies on-the-fly based on case-by-case geometry and transmitter velocity. This is foreseen as part of the LIO mission design [4]. In the following it is assumed that it will be possible to shift the internal transmitter frequency such that the desired frequency, f_0, appears in the ECEF frame. Neglecting relativistic effects (giving rise to an additional relative Doppler shift on the order of 10^{-10}), the internally generated frequency could be determined as

$$f_{\mathrm{Tx}} = f_0\left(1 - \frac{\vec{u}_{\mathrm{Tx}} \cdot (\vec{v}_{\mathrm{Tx}} - \vec{v}_{\Omega})}{c}\right), \tag{2.4}$$

where $\vec{u}_{\mathrm{Tx}}$ is a unit vector in the direction of the propagation at the transmitter, and $\vec{v}_{\Omega}$ could be the velocity vector of Earth's rotation at the transmitter (for a straight line originating at the transmitter in the direction of $\vec{u}_{\mathrm{Tx}}$, it can be shown that $\vec{u}_{\mathrm{Tx}} \cdot \vec{v}_{\Omega}$ is the same anywhere along the line although $\vec{v}_{\Omega}$ varies along the line). With this, the wind-induced Doppler shift can be written as

$$\Delta f_{\mathrm{w}} = -f_0 \frac{\vec{u} \cdot \vec{v}_{\mathrm{w}}}{c} = -f_0 \frac{\vec{u} \cdot \vec{v}}{c} = -f_0 \frac{v_{\shortparallel}}{c}, \tag{2.5}$$

where $\vec{u}$ is a unit vector along a ray path at a given point, $\vec{v}_{\mathrm{w}}$ is the 3D wind velocity vector at this point, $\vec{v}$ is its projection into the occultation plane, and $v_{\shortparallel}$ is the l.o.s. wind speed introduced in (2.3).

2.2 Considerations about spherical symmetry

Adopting local spherical symmetry, we assume that the wind locally blows horizontally along spherical shells, or more precisely that the projection of the wind velocity vector into the occultation plane follows a great circle, corresponding to a constant wind speed, v, at any given altitude, z. In other words, in the neighborhood of the tangent location of an occultation event, the wind is assumed to exhibit only a radial dependence, $v(r)$, where r is the distance from the center of local spherical symmetry (the Earth's ellipsoidal shape is disregarded here, since assumed rectified to spherical symmetry beforehand already by a suitable oblateness correction [5]). While in this case the relation $\vec{u} \cdot \vec{v}_{\mathrm{w}} = v_{\shortparallel} = v$ will hold at the tangent point of a ray path, $v_{\shortparallel}$ will otherwise

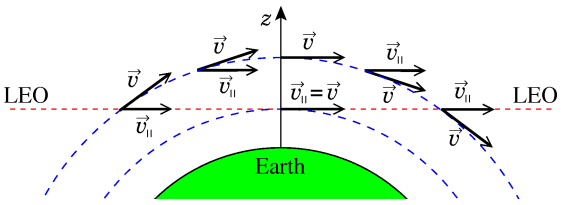

Figure 2.1 Illustration of a spherically symmetrical wind velocity, symbolized by $\vec{v}$ (here illustrated as being constant with altitude, z, along spherical shells; blue-dashed), and its projection, $\vec{v}_{\shortparallel}$, along a ray path (red-dashed) between two LEO platforms.

differ from v, and vary both along the ray path and along a given spherical shell. The relation and difference between the vectors $\vec{v}_{\shortparallel}$ and $\vec{v}$ is illustrated in Fig. 2.1. While $\vec{v}$ is the projection of $\vec{v}_{\rm w}$ into the occultation plane, $\vec{v}_{\shortparallel}$ is the projection of $\vec{v}$ (or $\vec{v}_{\rm w}$) onto the propagation direction (which in reality is slightly bended, though not illustrated as such); $v_{\shortparallel} = |\vec{v}_{\shortparallel}|$ and $v = |\vec{v}|$.

Although the variation of $v_{\shortparallel}$ along a given spherical shell is small, and in practice probably smaller than physical wind variations in general, it is a systematic variation that needs to be accounted for, since we are interested in the vertical wind profile, $v(z)$, that is attributable to the tangent point trajectory of the occultation event. As we will see below, the Abel transform that we can derive will be slightly different if we directly assume $v_{\shortparallel}$ (rather than v) to be spherically symmetrical. While the difference is small, the direct solution for $v_{\shortparallel}$ would be slightly biased, since it would be a solution that implicitly assumes that the wind speed in the occultation plane is slightly smaller at the tangent point than at other points on the great circle that includes the tangent point.

For the sake of detailed understanding, we derive below formulae for both solutions, i.e., for the retrieval of v (the appropriate solution that we focus on) and for the retrieval of $v_{\shortparallel}$ (as a side check), respectively. We shall refer to both $v_{\shortparallel}$ and v as the l.o.s. wind, since their true values are identical at the tangent point to which we attribute their solutions, but their different definitions should be kept in mind.

2.3 Formulae for retrieving the line-of-sight wind

The optical depth, τ, of a LIO measurement is theoretically given by

$$\tau = \int_{\rm Tx}^{\rm Rx} k {\rm d}s, \tag{2.6}$$

where k is the volume absorption coefficient and the integration is along the ray path. The volume absorption coefficient is a function of frequency, pressure, temperature, humidity, and trace gas species. For the wind retrieval, two frequencies, $f_{\rm w1}$ and $f_{\rm w2}$, on each side of the line center of the $C^{18}OO$ absorption line, where the derivative with respect to frequency is the largest, is envisaged to be used [2]. Inspired by the approach of [3], we can write the volume absorption coefficient for a frequency f_1 close to $f_{\rm w1}$ as

$$k(f_1) = k(f_{\rm w1}) + \frac{{\rm d}k}{{\rm d}f}\Big|_{f_{\rm w1}} (f_1 - f_{\rm w1}), \tag{2.7}$$

and likewise for a frequency f_2 close to $f_{\rm w2}$. If f_1 and f_2 are effective frequencies shifted from $f_{\rm w1}$ and $f_{\rm w2}$, respectively, because of the wind-induced Doppler shift, we have

$$k(f_1) = k(f_{\rm w1}) - f_{\rm w1}\frac{{\rm d}k}{{\rm d}f}\Big|_{f_{\rm w1}} \frac{v_{\shortparallel}}{c}, \tag{2.8}$$

and likewise for f_2. Introducing $\Delta k_0 = k(f_{\rm w2}) - k(f_{\rm w1})$ and $\Delta\chi_0 = f_{\rm w2}\frac{{\rm d}k}{{\rm d}f}\big|_{f_{\rm w2}} - f_{\rm w1}\frac{{\rm d}k}{{\rm d}f}\big|_{f_{\rm w1}}$, the difference between the absorption coefficients becomes

$$\Delta k = k(f_2) - k(f_1) = \Delta k_0 - \Delta\chi_0 \frac{v_{\shortparallel}}{c}, \tag{2.9}$$

and the optical depth difference can be written as

$$\Delta\tau = \int_{\mathrm{Tx}}^{\mathrm{Rx}} \Delta k_0 \mathrm{d}s - \frac{1}{c}\int_{\mathrm{Tx}}^{\mathrm{Rx}} \Delta\chi_0 v_{\shortparallel} \mathrm{d}s. \tag{2.10}$$

Thus Δk_0 and $\Delta\chi_0$ are differential parameters in the case of no wind, and in the following these are assumed to be known, e.g., from independent measurements of the $C^{18}OO$ concentration (using a frequency on the line center and a reference frequency further away) and other parameters. Since $f_{\mathrm{w}1}$ and $f_{\mathrm{w}2}$ are very close, unwanted effects, such as scintillations and defocusing, are removed to a very high degree in $\Delta\tau$ from real measurements.

2.3.1 Assuming v to be spherically symmetrical

The formulae in this section are based on the assumption that $v = v(r)$ (besides the assumption that $n = n(r)$ and $\Delta k_0 = \Delta k_0(r)$), which is the physically appropriate spherical symmetry assumption given that atmospheric dynamics at horizontal scales larger than about 10 km closely fulfill hydrostatic conditions in the vertical, leading to two-dimensional horizontal wind fields with comparatively negligble vertical wind velocities [6]. Then, according to Bouguer's law, $v_{\shortparallel} = \frac{av(r)}{rn(r)}$ and $\mathrm{d}s = \frac{rn(r)\mathrm{d}r}{\sqrt{r^2n^2(r)-a^2}}$. Making the substitution $x = rn(r)$, we can write

$$\Delta\tau(a) = 2\int_a^\infty \frac{x\Delta k_0(x)\frac{\mathrm{d}r}{\mathrm{d}x}\mathrm{d}x}{\sqrt{x^2-a^2}} - 2\frac{a}{c}\int_a^\infty \frac{\Delta\chi_0(x)v(x)\frac{\mathrm{d}r}{\mathrm{d}x}\mathrm{d}x}{\sqrt{x^2-a^2}}. \tag{2.11}$$

Ignoring (for the moment only) Δk_0, we can solve for v using an Abel transform:

$$v(a) \approx \frac{c}{\pi\Delta\chi_0(a)}\frac{\mathrm{d}}{\mathrm{d}r}\int_a^\infty \frac{\Delta\tau(x)\mathrm{d}x}{\sqrt{x^2-a^2}}, \tag{2.12}$$

where (as usual) $r = \frac{a}{n}$. Ignoring Δk_0 is justified if $f_{\mathrm{w}1}$ and $f_{\mathrm{w}2}$ is precisely located on each side of the line center, but this might not be the case in practice [3]. If $\Delta k_0 \neq 0$, but known, we can define, and in principle compute

$$\delta(a) = 2\int_a^\infty \frac{x\Delta k_0(x)\frac{\mathrm{d}r}{\mathrm{d}x}\mathrm{d}x}{\sqrt{x^2-a^2}}, \tag{2.13}$$

such that

$$v(a) = \frac{c}{\Delta\chi_0(a)}\frac{1}{\pi}\frac{\mathrm{d}}{\mathrm{d}r}\int_a^\infty \frac{(\Delta\tau(x)-\delta(x))\mathrm{d}x}{\sqrt{x^2-a^2}}. \tag{2.14}$$

However, we can also write

$$\delta(a) = 2\int_a^\infty \frac{a\Delta k_0(x)\frac{\mathrm{d}r}{\mathrm{d}x}\mathrm{d}x}{\sqrt{x^2-a^2}} + \varepsilon(a), \tag{2.15}$$

where

$$\varepsilon(a) = 2\int_a^\infty \frac{\sqrt{x-a}}{\sqrt{x+a}}\Delta k_0(x)\frac{\mathrm{d}r}{\mathrm{d}x}\mathrm{d}x. \tag{2.16}$$

Since the first term on the right-hand-side of (2.15) is almost identical to that of (2.13) (the difference being an a instead of the first x in the numerator of the integrand), $\varepsilon(a)$ is relatively small (and Δk_0 is already small by design). Ignoring $\varepsilon(a)$, we can derive an approximate expression for $v(a)$ without having to compute $\delta(a)$, but instead use directly the knowledge of $\Delta k_0(a)$:

$$v(a) \approx \frac{c}{\Delta\chi_0(a)}\Big[\frac{1}{\pi}\frac{\mathrm{d}}{\mathrm{d}r}\int_a^\infty \frac{\Delta\tau(x)\mathrm{d}x}{\sqrt{x^2-a^2}} + \Delta k_0(a)\Big]. \tag{2.17}$$

2.3.2 Side check: Assuming $v_{\shortparallel}$ to be spherically symmetrical

The formulae in this section are based on the assumption that $v_{\shortparallel} = v_{\shortparallel}(r)$. Then $\Delta k = \Delta k(r)$ and

$$\Delta\tau(a) = 2\int_a^\infty \frac{x\Delta k(x)\frac{\mathrm{d}r}{\mathrm{d}x}\mathrm{d}x}{\sqrt{x^2-a^2}}, \tag{2.18}$$

with the inverse solution [7]:

$$\Delta k(a) = -\frac{1}{\pi}\frac{1}{a}\frac{\mathrm{d}}{\mathrm{d}r}\int_a^\infty \frac{x\Delta\tau(x)\mathrm{d}x}{\sqrt{x^2-a^2}}. \tag{2.19}$$

Applying (2.9), we arrive at

$$v_{\shortparallel}(a) = \frac{c}{\Delta\chi_0(a)}\Big[\frac{1}{\pi}\frac{1}{a}\frac{\mathrm{d}}{\mathrm{d}r}\int_a^\infty \frac{x\Delta\tau(x)\mathrm{d}x}{\sqrt{x^2-a^2}} + \Delta k_0(a)\Big]. \tag{2.20}$$

Comparing this to (2.17), we see a difference (x instead of a) similar to the one leading to $\varepsilon(a)$ (cf. (2.13) and (2.15)), which was ignored. However, whereas Δk_0 (in (2.13)) is presumably small by design, $\Delta\tau$ (in (2.20)) can be appreciable when there is wind. Thus, when the wind is blowing the difference between $v_{\shortparallel}(a)$ and $v(a)$ is likely to be larger than the term that was ignored to get to $v(a)$ in (2.17). Although the solution for $v_{\shortparallel}(a)$ is a useful side check, $v(a)$ is the physically appropriate quantity as discussed above. Thus, in the initial performance assessment below, we focus on analyzing the accuracy and suitability of the formulation for $v(a)$, with some comparisons to $v_{\shortparallel}(a)$ as given by (2.20).

3 Numerical results

3.1 Absorption and transmission spectra

The volume absorption coefficient spectrum near the $C^{18}OO$ absorption line, for a series of tangent point heights, is shown in the left panel of Fig. 3.1. The spectrum is based on the HITRAN database (http://www.cfa.harvard.edu/hitran) [8] and the information available at http://hitran.iao.ru. The line shape is the Voigt line shape, which is the convolution between the Lorentz (pressure broadening) and the Gaussian (Doppler broadening) line shapes [9]. It is here calculated numerically using a high accuracy implementation of the Faddeeva function [10; 11] (using the expansion of [10], Eq. 38(I), with $N = 32$ terms, together with Eq. 39 with $M = 64$). The atmosphere was taken to be isothermal with a constant temperature of 240 K, a pressure scale height of 7 km, a CO_2 mixing ratio of 380 ppmv, and a $C^{18}OO$ abundance (relative to the CO_2 content) of 0.42%. The line center is at 4767.041455 cm^{-1} and the two anticipated wind retrieval channels are marked $\pm 0.004\,cm^{-1}$ on each side of the line center (vertical lines in the figure). The right panel of Fig. 3.1 shows the corresponding transmission spectrum ($-10\tau \log(e)$; in dB) calculated by the Abel integral assuming straight-line propagation (similar to (2.18), but for τ and k instead of $\Delta\tau$ and Δk, and with $\frac{dr}{dx} = 1$). This can be compared to a similar figure in [3] and [4]. The differences to those works are only noticeable for the lowest tangent point heights and can be attributed to the straight-line propagation used here. Details on the numerical implementation of the Abel integral to calculate the optical depths (as well as $\varepsilon(a)$ in (2.16)) are described in Appendix A.1.

Figure 3.2 shows the derivatives of the spectra in Fig. 3.1. For the transmission spectrum (right), this confirms the result from the earlier works mentioned above that the inflection points, where the derivatives are maximum or minimum, are located close to the anticipated wind retrieval channels, and more or less independent of tangent point height (TPH). This should ensure maximum sensitivity to the wind-induced Doppler

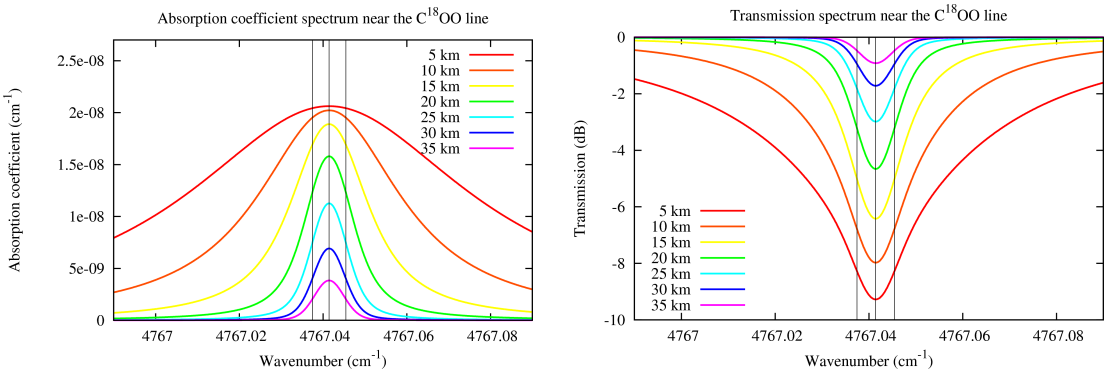

Figure 3.1 Absorption coefficient spectrum around the $C^{18}OO$ absorption line (left), and the corresponding transmission spectrum (right) for a series of tangent point heights between 5 and 35 km.

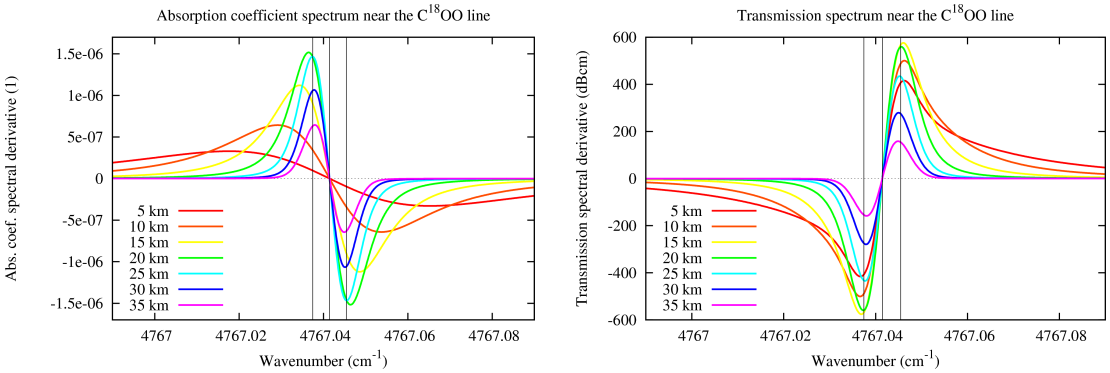

Figure 3.2 First derivatives of the absorption coefficient spectrum (left) and the transmission spectrum (right) based on the spectra in Fig. 3.1. Note that the units of the spectral derivatives of the absorption coefficient and the transmission are $[\mathrm{cm}^{-1}/\mathrm{cm}^{-1}]=[1]$ and $[\mathrm{dB}/\mathrm{cm}^{-1}]=[\mathrm{dBcm}]$, respectively.

shift. However, for the volume absorption coefficient spectrum (left), the inflection points depend on the TPH, and are only near the wind retrieval channels at the higher altitudes. Thus, it becomes relevant to assess, not only the error we make if we ignore $\varepsilon(a)$ to get to $v(a)$ in (2.17), but also the size of the higher order terms neglected in the series expansion of Δk in (2.9).

3.2 Wind retrieval error terms

Taking into account $\varepsilon(a)$ as well as the second and third order derivatives in the series expansion of Δk, a quite accurate, iterative formula for the l.o.s. wind can be written as

$$v(a) = \frac{c}{\Delta\chi_0(a)}\Big[\frac{1}{\pi}\frac{\mathrm{d}}{\mathrm{d}r}\int_a^\infty \frac{(\Delta\tau(x)-\varepsilon(x))\mathrm{d}x}{\sqrt{x^2-a^2}} + \Delta k_0(a) + \Big(\frac{v(a)}{c}\Big)^2\Delta\zeta_0(a) - \Big(\frac{v(a)}{c}\Big)^3\Delta\xi_0(a)\Big], \tag{3.1}$$

where $\Delta\zeta_0 = \frac{1}{2}f_{\mathrm{w}2}^2\frac{\mathrm{d}^2k}{\mathrm{d}f^2}\big|_{f_{\mathrm{w}2}} - \frac{1}{2}f_{\mathrm{w}1}^2\frac{\mathrm{d}^2k}{\mathrm{d}f^2}\big|_{f_{\mathrm{w}1}}$ and $\Delta\xi_0 = \frac{1}{6}f_{\mathrm{w}2}^3\frac{\mathrm{d}^3k}{\mathrm{d}f^3}\big|_{f_{\mathrm{w}2}} - \frac{1}{6}f_{\mathrm{w}1}^3\frac{\mathrm{d}^3k}{\mathrm{d}f^3}\big|_{f_{\mathrm{w}1}}$. Besides even higher order derivative terms than the ones included here, very small terms related to $\Delta\zeta_0$ and $\Delta\xi_0$, somewhat akin to how ε is related to Δk_0 (cf. (2.16)), were ignored to obtain (3.1). In order of appearance, the extra terms, when comparing this to the approximate expression in (2.17), will be termed ε-term, ζ-term, and ξ-term. These terms are measured in units of velocity (i.e., including the factor $\frac{c}{\Delta\chi_0(a)}$), and they all contribute a little to the l.o.s. wind, or give rise to small systematic errors in the retrieval if ignored. Likewise, $\frac{c}{\Delta\chi_0(a)}\Delta k_0(a)$ will be referred to as the k-term. Since $f_{\mathrm{w}2}^2\frac{\mathrm{d}^2k}{\mathrm{d}f^2}\big|_{f_{\mathrm{w}2}} \approx f_{\mathrm{w}1}^2\frac{\mathrm{d}^2k}{\mathrm{d}f^2}\big|_{f_{\mathrm{w}1}}$, whereas $f_{\mathrm{w}2}^3\frac{\mathrm{d}^3k}{\mathrm{d}f^3}\big|_{f_{\mathrm{w}2}} \approx -f_{\mathrm{w}1}^3\frac{\mathrm{d}^3k}{\mathrm{d}f^3}\big|_{f_{\mathrm{w}1}}$, $\Delta\zeta_0(a)$ can be much smaller than $\Delta\xi_0(a)$, and the ζ-term and the ξ-term may be of the same order of magnitude. This depends on the precise location of $f_{\mathrm{w}1}$ and $f_{\mathrm{w}2}$ on each side of the absorption line center. The extra terms could in principle be included in a solution without much ado, and (3.1) could be solved iteratively with (2.17) as a first guess (possibly including

the ε-term already), but it may not be worthwhile in practice since the error we make by ignoring these terms is quite small. This was verified by numerical simulations shown in the next section.

3.3 Residual error assessment

The results in this section are based on the absorption and transmission spectra with the parameters and simplifications described in Section 3.1. To illustrate the possible contribution of different terms in (3.1) to the error of a wind retrieval using (2.17), the wave numbers ($\nu = f/c$) corresponding to f_{w1} and f_{w2} were offset by $0.000045\,\mathrm{cm}^{-1}$ from the ideal values to get appreciable sizes of Δk_0 and $\Delta\zeta_0$, i.e., $\nu_{\mathrm{w1}} = 4767.0375\,\mathrm{cm}^{-1}$ and $\nu_{\mathrm{w2}} = 4767.0455\,\mathrm{cm}^{-1}$. This corresponds to a relative shift of $+10^{-8}$, comparable to the knowledge and stability requirements of a possible future LIO mission [4; 2]. The forward modeling of the optical depths were based on the Abel integral (again similar to (2.18), but for τ and k, and with $\frac{\mathrm{d}r}{\mathrm{d}x} = 1$), taking into account the modification of the absorption coefficient because of the wind-induced Doppler shift (via $v_{\shortparallel} = \frac{a}{x}v(x)$). The integral in (2.17) (and the one for the ε-term in (3.1)) was solved numerically as described in Appendix A.2.

The left panel of Fig. 3.3 shows the result of a simulation with a constant wind speed of 30 m/s, independent of altitude. The different terms are here plotted with the opposite sign of that in (3.1) to illustrate the error made if they are ignored. The k-term is about 3 m/s (shown here as 1% of its total) and thus constitutes just about 10% of the total wind in this case, whereas the other terms and the retrieval error we get by ignoring them, are on the order of 0.1 m/s, i.e., ∼0.3%. The latter is truly negligible compared to the k-term, which already would be close to the measurement resolution according to the knowledge and stability requirements (more precisely, the measurement resolution is $\sim$ 1 m/s given the stability requirement of $1 \cdot 10^{-8}(3\sigma) \equiv \frac{1}{3} \cdot 10^{-8}(1\sigma)$ specified in [4]). The residual error if we include all of these small terms in the solution is less than

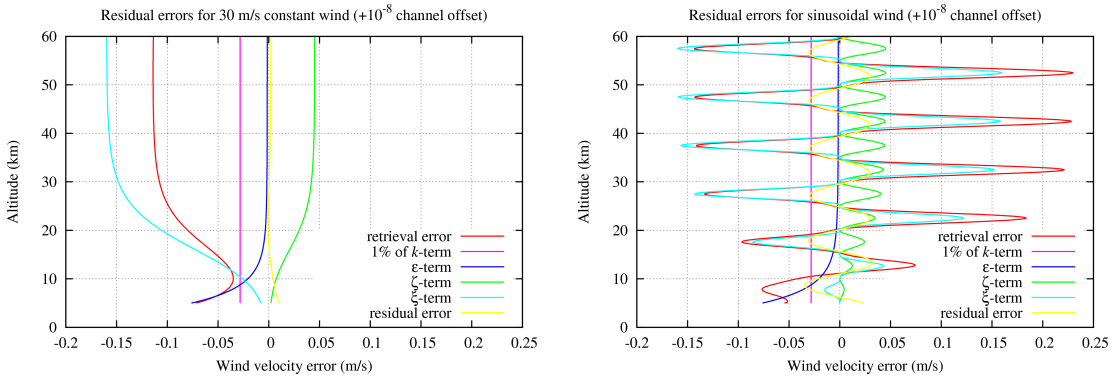

Figure 3.3 Residual errors in the retrieval of simple wind profiles. Left: for a constant wind velocity of 30 m/s. Right: for a sinusoidal alternation of the wind with altitude (cf. Fig. 3.4). For reference, the magenta vertical lines show 1% of the k-term, and the yellow curves are the residual errors if all the other terms are accounted for in the retrievals.

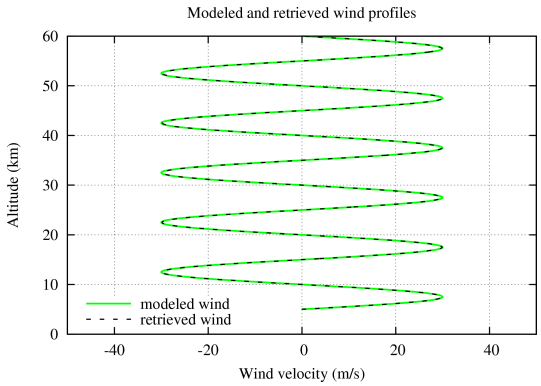

Figure 3.4 Modeled and retrieved wind profiles in the case of a sinusoidal alternation of the wind with altitude.

0.01 m/s (yellow curve) and is possibly due to the terms neglected in deriving (3.1). The right panel of Fig. 3.3 shows the corresponding results for the sinusoidal wind profile in Fig. 3.4 (inspired by the work of [3]). The ε-term is the same since it is independent of the solution and depends only on Δk_0, whereas other residual terms depend on the alternating wind with altitude. The residual error if we include all the terms in the solution (yellow curve) is here about 0.1% of the true wind profile (with opposite sign), and is mainly due to the discretization (100 m intervals) in the numerical integration and differentiation in (3.1). This was verified by increasing the vertical resolution by a factor of two, which reduced the residual error by a factor of four.

Figure 3.5 shows the retrieval errors using either (2.17) (termed v-retrieval) or (2.20) (termed $v_{\shortparallel}$-retrieval), for 30 and 5 m/s constant winds, as well as the alternating wind profile in Fig. 3.4. The left panel shows the results with the relative shift of ν_{w1} and ν_{w2} being $+10^{-8}$ as discussed above, whereas the right panel shows the results if $\nu_{w1} = 4767.037\,\mathrm{cm}^{-1}$ and $\nu_{w2} = 4767.045\,\mathrm{cm}^{-1}$, corresponding to a relative shift of -10^{-7}. With the channel offset at a magnitude of 10^{-8}, we see that the retrieval error for the $v_{\shortparallel}$-retrieval is significantly larger than that of the v-retrieval if the wind velocity is 30 m/s, especially below 20 km, but comparable to the v-retrieval if the wind velocity

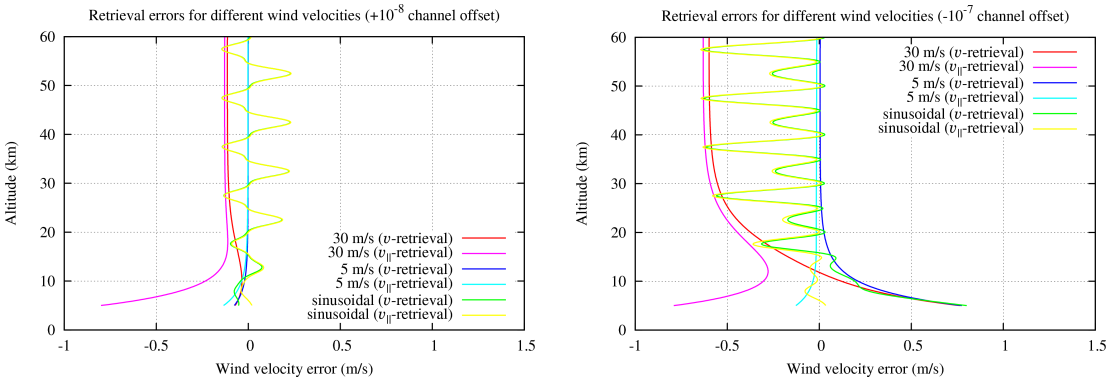

Figure 3.5 Retrieval errors for different wind profiles using either (2.17) or (2.20). Left: for a relative channel offset of $+10^{-8}$. Right: for a relative channel offset of -10^{-7}.

is 5 m/s or alternating with altitude. With the channel offset at a magnitude of 10^{-7}, the v-retrieval always has a large error below 15 km, which is dominated by the ε-term (being independent of the wind velocity, but proportional to the general size of the k-term). This is comparable to the error of the v_{II}-retrieval for a 30 m/s constant wind, but as the wind becomes smaller, or alternating with altitude, the error of the v_{II}-retrieval is smaller below 15 km. However, as mentioned above, the ε-term could be taken into account in the v-retrieval without much ado, significantly reducing the already small error below 15 km, whereas the error in the v_{II}-retrieval is more fundamental because the v_{II}-retrieval is based on the (on average) false assumption that v_{II} is spherically symmetrical (cf. Section 2.2).

In any case, the retrieval errors, even if the magnitude of the relative shift of the wind retrieval channels is 10^{-7}, is smaller than the error that we would face in practice according to the knowledge and stability requirements (giving rise to an uncertainty in the knowledge of the k-term of about 1 m/s).

4 Conclusion

Different formulae involving Abel transforms have been developed and analysed for the retrieval of the line-of-sight wind profile from future LEO-LEO IR laser occultation measurements. The simplest formula is given by (2.17). Assuming spherical symmetry, numerical simulations using the $C^{18}OO$ absorption line with the line center at $4767.041455\,\mathrm{cm}^{-1}$, show that the error using this formula is on the order of 0.1 m/s. Details depend on the l.o.s. wind velocity and the shift of the two transmitted wind retrieval channels with respect to their nominal values (the nominal values here taken to be $\pm 0.004\,\mathrm{cm}^{-1}$ on each side of the line center). The relative shift of the retrieval channels were assumed to be 10^{-8}. If the relative shift is instead 10^{-7}, the maximum retrieval error will be about 0.5 m/s, which is still smaller than the error expected according to the knowledge and stability requirements of a future instrument (being about 1 m/s, corresponding to a relative shift of within 10^{-8} only). If needed in future applications, a very accurate, but more elaborate formula is given by (3.1).

The next step will be an implementation of this new Abel transform-based wind retrieval in the EGOPS/xEGOPS software [12], in order to subsequently analyze the performance of the LIO wind profiling in detail by way of quasi-realistic end-to-end simulations.

Acknowledgments The authors thank V. Proschek and A. Plach from the AEXPWIND team at the Wegener Center, University of Graz (AT), for valuable discussions on the work and this report. Access to the HITRAN database was provided by L. Rothman (Harvard Univ., USA) via www.cfa.harvard.edu/hitran. This work was funded by ESA under the AEXPWIND project (ESA/ESTEC Contract No. 4000105679/12/NL/CBi).

Appendix

A Numerical solutions to Abel integrals

A.1 Forward Abel integral

Equation (2.18), with τ and k instead of $\Delta\tau$ and Δk, and with $\frac{\mathrm{d}r}{\mathrm{d}x} = 1$, reads:

$$\tau(a) = 2\int_a^\infty \frac{xk(x)\mathrm{d}x}{\sqrt{x^2 - a^2}}. \tag{A.1}$$

For accurate numerical implementation we can introduce the change of variable $y = \exp(-\frac{\sqrt{x^2-a^2}}{b})$, where b is a constant (in units of length) to be determined below. Thus, (A.1) can be written

$$\tau(a) = 2b\int_0^1 \frac{k(x(y))}{y}\mathrm{d}y, \tag{A.2}$$

where $x(y) = \sqrt{a^2 + (b\ln y)^2}$. The upper limit ($y = 1$) corresponds to $x = a$ where the integrand has a finite value (as opposed to (A.1)). To show that the integrand, with appropriate choice of b, also has a finite value (in fact 0) at the lower limit, we can make the assumption that $k(x)$ falls off exponentially with height for large x, i.e., $k(x) \sim \exp(-\frac{x}{H})$, where H is a scale height at high altitudes. With this assumption, we see that $\frac{k(x)}{y} \sim \exp(\frac{\sqrt{x^2-a^2}}{b} - \frac{x}{H}) \to 0$ for $x \to \infty$, if $b > H$. In practice, most accurate results are obtained if b is chosen such that the integrand is appreciable in a considerable part of the interval between 0 and 1, but with a not too abrupt transition to near zero for $y \to 0$. In the numerical implementation here, $b = 300\,\mathrm{km}$. Setting $\frac{k(x)}{y} = 0$ at the lower limit, (A.2) was solved numerically using the composite Simpson's rule with a sufficient number of subintervals between 0 and 1 (in the simulations in this work, 1000 subintervals of size $h = 0.001$ was sufficient to ensure high enough accuracy in all cases such that the discretization errors in the forward model were negligible in the wind retrieval results; the discretization error of the composite Simpson's rule is proportional to h^4).

For illustration, Fig. A.1 shows examples of the integrand of (A.2), with $b = 300\,\mathrm{km}$, for four different values of the TPH. The volume absorption coefficient, $k(x)$, was based on the HITRAN database with the characteristics of the atmosphere given in Section 3.1, and for a frequency corresponding to $\nu_{\mathrm{w1}} = 4767.037455\,\mathrm{cm}^{-1}$. The solid curves are for a case without wind, whereas the dashed curves are for a case where the frequency, and thereby the volume absorption coefficient, is modified due to a sinusoidal wind profile (cf. Fig. 3.4). The numerical computation of the optical depth for each TPH (accurately evaluating the forward Abel integral to infinity), amounts to finding the area under each of the curves.

The same change of variable can be applied for the numerical integration involving other functions than $k(x)$, as long as the function approximately falls off exponentially with altitude, e.g., in the numerical computations of bending angle from refractive index in simulations of GNSS radio occultation measurements. In principle, the same change of variable could also be applied in the so-called inverse Abel integral, solving for the

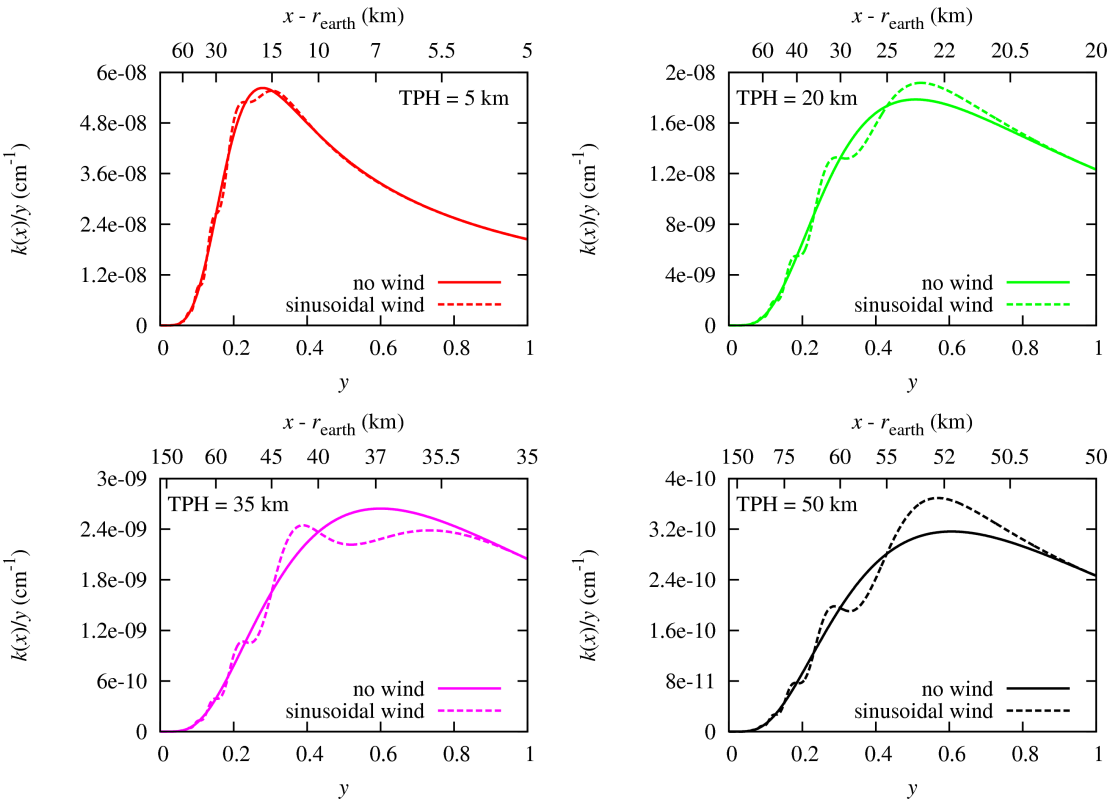

Figure A.1 Examples of the integrand of (A.2) for four different values of the TPH.

wind profile and the absorption coefficient difference in equations (2.17) and (2.19), or when deriving the refractive index from bending angle in GNSS radio occultation measurements. However, simulated (or real) measurements are not available to infinite altitudes, so one would have to augment the data with some analytical expression to infinity, e.g., via statistical optimization or simple extrapolation. Such additional effort was not made here. Instead, an alternative approach for solving the inverse Abel integral is described in Appendix A.2.

A.2 Inverse Abel integral

Assuming $\Delta\tau(x) = 0$ at some high altitude (corresponding to $x = a_{\text{top}}$) and above, we define $\kappa(a)$ as an approximation to the integral in (2.17):

$$\kappa(a) \equiv \int_a^{a_{\text{top}}} \frac{\Delta\tau(x)\mathrm{d}x}{\sqrt{x^2 - a^2}}. \tag{A.3}$$

Splitting up the integration into a sum of sub-integrals, we can write

$$\kappa(a) = \sum_{j=i}^{n} \int_{a_j}^{a_{j+1}} \frac{\Delta\tau(x)\mathrm{d}x}{\sqrt{x^2 - a^2}}, \tag{A.4}$$

where $a_i = a$, $a_{n+1} = a_{\text{top}}$, and $a_{j+1} > a_j$. Further, making the approximation that $\Delta\tau(x)$ varies linearly with x in each sub-integral, they can be solved analytically. After some effort (see [13]) we get:

$$\begin{aligned}\kappa(a_i) = &-\frac{1}{\Delta a_i}\left[\sqrt{a_{i+1}^2 - a_i^2} - a_{i+1}\ln\Big(\frac{a_{i+1} + \sqrt{a_{i+1}^2 - a_i^2}}{a_i}\Big)\right]\Delta\tau(a_i) \\ &+ \sum_{j=i+1}^{n}\left\{\frac{1}{\Delta a_{j-1}}\left[\sqrt{a_j^2 - a_i^2} - \sqrt{a_{j-1}^2 - a_i^2} - a_{j-1}\ln\Big(\frac{a_j + \sqrt{a_j^2 - a_i^2}}{a_{j-1} + \sqrt{a_{j-1}^2 - a_i^2}}\Big)\right]\right. \\ &\left. - \frac{1}{\Delta a_j}\left[\sqrt{a_{j+1}^2 - a_i^2} - \sqrt{a_j^2 - a_i^2} - a_{j+1}\ln\Big(\frac{a_{j+1} + \sqrt{a_{j+1}^2 - a_i^2}}{a_j + \sqrt{a_j^2 - a_i^2}}\Big)\right]\right\}\Delta\tau(a_j),\end{aligned} \tag{A.5}$$

where $\Delta a_j = a_{j+1} - a_j$. As noted by [14], significant numerical precision may be lost using such expression, because nearly equal terms are subtracted from each other. A form that better preserves numerical precision is obtained by introducing $\epsilon_k = \frac{(a_{i+k} - a_i)}{a_i}$ for a given i ($k = j - i$; not to be confused with the volume absorption coefficient). Equation (A.5) can then be written

$$\begin{aligned}\kappa(a_i) = &-\epsilon_1^{-1}\left[\sqrt{\epsilon_1(2+\epsilon_1)} - (1+\epsilon_1)\ln\Big(1 + \epsilon_1 + \sqrt{\epsilon_1(2+\epsilon_1)}\Big)\right]\Delta\tau(a_i) \\ &+ \sum_{k=1}^{n-i}\left\{(\epsilon_k - \epsilon_{k-1})^{-1}\left[\sqrt{\epsilon_k(2+\epsilon_k)} - \sqrt{\epsilon_{k-1}(2+\epsilon_{k-1})}\right.\right. \\ &\left. - (1+\epsilon_{k-1})\ln\Big(\frac{1 + \epsilon_k + \sqrt{\epsilon_k(2+\epsilon_k)}}{1 + \epsilon_{k-1} + \sqrt{\epsilon_{k-1}(2+\epsilon_{k-1})}}\Big)\right] \\ &- (\epsilon_{k+1} - \epsilon_k)^{-1}\left[\sqrt{\epsilon_{k+1}(2+\epsilon_{k+1})} - \sqrt{\epsilon_k(2+\epsilon_k)}\right. \\ &\left.\left. - (1+\epsilon_{k+1})\ln\Big(\frac{1 + \epsilon_{k+1} + \sqrt{\epsilon_{k+1}(2+\epsilon_{k+1})}}{1 + \epsilon_k + \sqrt{\epsilon_k(2+\epsilon_k)}}\Big)\right]\right\}\Delta\tau(a_{i+k}).\end{aligned} \tag{A.6}$$

This form was used to compute the integrals in (2.17) and (3.1) for a number of a_i values (the atmosphere was divided into $n = 1000$ layers of thickness $h = 100\,\text{m}$ between 5 and 105 km; the discretization error of the approach is consistent with that of the following derivative operation in those equations, which is proportional to h^2). The same form was also used to compute the integral in (2.20) just with $x\Delta\tau(x)$ replacing $\Delta\tau(x)$ (i.e., assuming that $x\Delta\tau(x)$ varies linearly with x in each sub-integral).

References

[1] Kirchengast, G., and AEXPWIND proposal team (2012), AEXPWIND: Study of trace gas retrieval and performance of wind and greenhouse gas profiling in the Irdas-Exp/Accurate context—summary input for negotiation meeting, WEGC Tech. Note to ESA/ESTEC Mar. 2012, Wegener Center for Climate and Global Change, University of Graz, Graz, Austria

[2] Kirchengast, G., and S. Schweitzer (2011), Climate benchmark profiling of greenhouse gases and thermodynamic structure and wind from space, Geophys. Res. Lett., 38, L13701, doi:10.1029/2011GL047617

[3] Schweitzer, S. (2010), The ACCURATE concept and the infrared laser occultation technique: Mission design and assessment of retrieval performance, Ph.D. Thesis, Scientific Report 34-2010, Wegener Center for Climate and Global Change, University of Graz, Graz, Austria

[4] Kirchengast, G., and ACCURATE proposal team (2010), Accurate–climate benchmark profiling of greenhouse gases and thermodynamic variables and wind from space, ESA Earth Explorer Opportunity Mission EE8 Proposal, Scientific Report 36-2010, Wegener Center for Climate and Global Change, University of Graz, Graz, Austria

[5] Syndergaard, S. (1998), Modeling the impact of the Earth's oblateness on the retrieval of temperature and pressure profiles from limb sounding, J. Atmos. Solar-Terr. Phys., 60, 171–180

[6] Salby, M. L. (2012), *Physics of the Atmosphere and Climate*, Cambridge University Press, Cambridge-New York

[7] Schweitzer, S., G. Kirchengast, M. Schwaerz, J. Fritzer, and M. E. Gorbunov (2011), Thermodynamic state retrieval from microwave occultation data and performance analysis based on end-to-end simulations, J. Geophys. Res., 116, D10301, doi:10.1029/2010JD014850

[8] Rothman, L. S., I. E. Gordon, A. Barbe, D. C. Benner, et al. (2009), The HITRAN 2008 molecular spectroscopic database, Journal of Quantitative Spectroscopy and Radiative Transfer, 110, 533–572

[9] Liou, K. N. (2002), *An Introduction to Atmospheric Radiation*, Elsevier, San Diego, California

[10] Weideman, J. A. C. (1994), Computation of the complex error function, SIAM Journal on Numerical Analysis, 31, 1497–1518

[11] Abrarov, S. M., and B. M. Quine (2011), Efficient algorithmic implementation of the Voigt/complex error function based on exponential series approximation, Applied Mathematics and Computation, 218, 1894–1902

[12] Fritzer, J., G. Kirchengast, M. Pock, and V. Proschek (2010), End-to-end generic occultation performance simulation and processing system version 5.5 (EGOPS and xEGOPS) software user manual, Tech. Rep. ESA-ESTEC WEGC-EGOPS-2012-TR01, Wegener Center and IGAM/Inst. of Physics, University of Graz, Graz, Austria

[13] Syndergaard, S. (1999), Retrieval analysis and methodologies in atmospheric limb sounding using the GNSS radio occultation technique, Scientific Report 99-6, Danish Meteorological Institute, Copenhagen, Denmark

[14] Lei, J., S. Syndergaard, A. G. Burns, S. C. Solomon, et al. (2007), Comparison of COSMIC ionospheric measurements with ground-based observations and model predictions: preliminary results, J. Geophys. Res., 112, A07308, doi:10.1029/2006JA012240